PAPER

Check for updates

Proton conductor NASICON-structure $Li_{1+x}Cd_{x/2}$ $Zr_{2-x/2}(PO_4)_3$ as solid electrolyte for intermediate-temperature fuel cells†

Xiuxiu Li,[a] Enyi Hu,[a] Faze Wang, [ID] *[a] Peter Lund,[b] Bin Zhu [ID] [a] and Jun Wang*[a]

Low ionic conductivity of solid electrolytes at intermediate temperatures hinders the commercialization process of solid fuel cell technology. A sodium superionic conductor (NASICON)-structure with a rigid three-dimensional network and an interconnected interstitial space is expected to be an ideal solid electrolyte for fuel cells. Based on the H^+/Li^+ exchange engineering strategy, here we report a NASICON-structure proton conductor $Li_{1+x}Cd_{x/2}Zr_{2-x/2}(PO_4)_3$ (x = 0.5, 1, 1.5, 2) derived from $CdZr_4(PO_4)_6$ to construct a fuel cell device. Among all samples, the $Li_3Cd_1Zr_1(PO_4)_3$ cell device exhibits a high performance including peak power density 815 mW cm^{-2}, proton conductivity 0.165 S cm^{-1} and activation energy 0.372 eV at 550 °C. Theoretical and experimental studies both suggest that the high proton conductivity benefits from the unique 3D interstitial space and rapid H^+/Li^+ exchange in the NASICON material. Under fuel cell operating conditions, the interstitial space of $Li_{1+x}Cd_{x/2}Zr_{2-x/2}(PO_4)_3$ (x = 2) substitutes mobile Li^+ with H^+ enabling fast proton transport. The new transport mechanism and excellent proton conductivity suggest that $Li_{1+x}Cd_{x/2}Zr_{2-x/2}(PO_4)_3$ provides new opportunities for enriching novel electrolyte materials in intermediate temperature protonic ceramic fuel cells (IT-PCFCs).

1. Introduction

A solid oxide fuel cell (SOFC) is an electrochemical device that can directly convert the chemical energy of hydrogen or another fuel to electrical energy through an electrochemical reaction without a conventional combustion process.[1–3] The fuel cell system has been utilized in a variety of energy applications.[4,5] The attractive characteristics make them quite fitting for addressing the energy crisis in the present situation of international energy development. Unfortunately, the large-scale commercialization of SOFCs is still challenging because of low ionic conductivity at high operating temperatures. Though proton conductors at lower temperatures have been proposed to promote the commercialization and future development of SOFCs,[6–8] intermediate temperature protonic ceramic fuel cells (IT-PCFCs) still face the challenge of how to guarantee high performance at lower temperatures. Therefore, novel-class electrolyte materials need to be further explored and discovered to meet the more stringent requirements.

Sodium superionic conductor NASICON (Na superionic conductor)-type oxide-based materials are considered to be one of the most promising solid electrolytes due to their reasonable high Li-ion conductivities at room temperature.[9–11] PO₄ tetrahedra and metal oxide octahedra constitute the three-dimensional connected crystal skeleton of NASICON electrolyte, and partial Li^+ fills the pores of the skeleton structure to construct three-dimensional connected ion transport channels. The essential structural feature of rigid and three-dimensional NASICON materials is an interconnected interstitial space that is occupied by mobile Li^+ ions.[12–14] These mobile lithium ions can migrate freely and exhibit certain ion conduction properties at room temperature.

In recent years, a study on the H^+/Li^+ exchange engineering strategy has been proposed to turn a lithium-ion conductor into a proton conductor. Li^+ ions can be substituted by H^+, which implies that protons can transport through existing interstitial Li^+ space to exhibit the proton conduction function.[15–17] The ion-exchange strategy has been applied to fast lithium-ion conductors including Garnet[18,19] and LISICON[20–23] structure materials. Chen *et al.*[20] reported that the $Li_{13.7}In_{0.2}Sr_{0.1}Zn(GeO_{4+\delta})_4$ material was successfully converted into a proton conductor and exhibited a proton conductivity of 0.094 S cm^{-1} in a hydrogen atmosphere at 600 °C. Matsui *et al.*[23] demonstrated that the $Li_{3.13}H_{0.37}Zn_{0.25}GeO_4$ conductor through the simple ion-exchange method could even obtain 5.5 mS cm^{-1} of electrical conductivity at 200 °C. As fast sodium-ion conductors with a similar structure, NASICON-structure materials are likely

a Jiangsu Provincial Key Laboratory of Solar Energy Science and Technology, School of Energy & Environment, Southeast University, Nanjing 210096, China. E-mail: fazewang@seu.edu.cn; wj-jw@seu.edu.cn

b Department of Engineering Physics/Advanced Energy Systems, School of Science, Aalto University, Aalto 00076, Finland

† Electronic supplementary information (ESI) available. See DOI: https://doi.org/10.1039/d3ta05182j

to benefit from this ion-exchange strategy. This strategy has been successfully applied to NASICON materials in reports from Stenina *et al.*[24,25] indicating the great potential to turn NASICON materials into proton conductor electrolytes. Lu *et al.*[26] reported that the Li vacancy generated after Li migration in NASICON materials provides the proton migration path under fuel cell conditions. However, the application of the interesting ion-exchange method on NASICON electrolytes is limited and needs further exploration.

Considering that the new proton transport mechanism may bring new opportunities and inject new vitality into the development of IT-PCFCs, from the perspective of the H^+/Li^+ engineering strategy, novel $Li_{1+x}Cd_{x/2}Zr_{2-x/2}(PO_4)_3$ ($x = 0.5, 1, 1.5, 2$) materials were designed as a proton electrolyte for IT-SOFCs, which have a rigid 3D interstitial space for proton transport and therefore enhance ion conductivity. In comparison to pristine $CdZr_4(PO_4)_6$, the effects of lithium content ($x = 0.5, 1, 1.5, 2$) in $Li_{1+x}Cd_{x/2}Zr_{2-x/2}(PO_4)_3$ on the crystal structure, electrochemical performance, and proton transport characteristics were studied. Our results demonstrated that the optimal component $Li_3Cd_1Zr_1(PO_4)_3$ is the promising electrolyte candidate for LT-PCFCs. DFT calculations predict the most probable H^+/Li^+ trajectories and confirm the proton transport mechanism in $Li_3Cd_1Zr_1(PO_4)_3$ complementing the experimental results. The novel proton transport mechanism has great potential in protonic conductor design and optimization for PCFC application.

2. Experimental section

2.1. Materials preparation

$Li_{1+x}Cd_{x/2}Zr_{2-x/2}(PO_4)_3$ ($x = 0.5, 1, 1.5, 2$) and $CdZr_4(PO_4)_6$ powder were synthesized by the sol–gel method with the precursors $ZrOCl_2 \cdot 6H_2O$ (Aldrich), $Cd(NO_3)_2 \cdot 4H_2O$ (Aldrich), Li_2CO_3 (Aldrich) and $NH_4H_2PO_4$ (Aldrich, 99.99%). Li_2CO_3 and $NH_4H_2PO_4$ were dissolved in deionized water at a stoichiometric ratio and stirred for half an hour. Then the solution was added dropwise to the $ZrOCl_2 \cdot 6H_2O$ and $Cd(NO_3)_2$ solution with continuous stirring. After evaporating the solvent at 80 °C, the resulting powder was heated at 450 °C in air for 10 hours to burn off volatiles. The final product was obtained after a secondary calcination step at 750 °C for 12 h in air.

2.2. Fuel cell fabrication and measurements

A symmetric cell with a single-cell configuration of Ni-NCAL/Electrolyte/NCAL-Ni was used for the electrochemical measurement. The as-prepared $Li_{1+x}Cd_{x/2}Zr_{2-x/2}(PO_4)_3$ and $CdZr_4(PO_4)_6$ were used as the electrolyte membrane and NCAL ($Ni_{0.8}Co_{0.15}Al_{0.05}Li$-oxide, B&M Science and Technology Co., Ltd, Tianjin, China) was pasted on the nickel foam and used as the electrode for the oxygen reduction reaction (ORR) and hydrogen oxidation reaction (HOR). NCAL powder was first mixed with absolute ethanol to form a black slurry, and then painted on the nickel foam with a thickness of 2 mm. The electrode was baked for 30 minutes at 100 °C to evaporate the solvent and obtain the final electrode for testing. In order to obtain the single fuel cell

NCAL-Ni/Electrolyte/NCAL-Ni with symmetrical configuration, $Li_{1+x}Cd_{x/2}Zr_{2-x/2}(PO_4)_3$ ($x = 0.5, 1, 1.5, 2$) and $CdZr_4(PO_4)_6$ powder were sandwiched between two same pieces of NCAL-Ni electrodes at a pressure over 200 Mpa. The obtained single cell device possesses 0.64 cm² effective working area and ∼1 mm thickness.

The as-fabricated fuel cells were fixed on a stainless-steel sample holder and then were preheated at 550 °C for 30 min before testing. During the performance test, hydrogen and ambient air served as fuel and an oxidizer with a flow velocity of 100 ml min⁻¹, respectively. The electrochemical impedance spectra (EIS) measurement was carried out on a CHI660E electrochemical work station (CH Instruments Ins.) in open circuit voltage (OCV) mode. During the EIS test, the AC voltage amplitude was 5 mV and frequency range was from 0.1 Hz to 1 MHz. The experimental impedance data were then fitted using the software Zview2. The *I–V* (current–voltage) and *I–P* (current-power) data of the cells at 460–550 °C were recorded using an IT8511 electronic load (ITECH Electrical Co., Ltd) using IT7000 software.

For the ion conductivity measurement of $Li_3Cd_1Zr_1(PO_4)_3$, Ag was used as the current collector instead of NCAL electrodes. The electrolyte powder was ground and pressed using the same manufacturing method as above. Both sides of the pellet were painted with Ag paste to fabricate the $Ag/Li_3Cd_1Zr_1(PO_4)_3/Ag$ device and then heated at 550 °C for 1 h. During the test, the pellets were assembled in the sample holder under different atmospheres (N_2/N_2, H_2/H_2 and air/air) and the EIS (or *I–t* curve) data were collected using the CHI660E electrochemical workstation.

2.3. Materials characterization

The phase structures of $Li_{1+x}Cd_{x/2}Zr_{2-x/2}(PO_4)_3$ ($x = 0.5, 1, 1.5, 2$) and $CdZr_4(PO_4)_6$ powder were identified using an X-ray diffractometer (Germany, Bruker Corporation) with Cu Kα radiation ($\lambda = 1.5418$ Å). The angular range of 2θ is between 10° and 40°, and the scanning step was 0.02°. Morphological properties of the synthesized samples were obtained by scanning electron microscopy (SEM, Thermo Scientific Apreo 2C). The cross-sectional structural morphology of the fuel cell was recorded by scanning electron microscopy (SEM, ZEISS Siama 500). High resolution transmission electron microscopy (HR-TEM) and energy dispersive X-ray spectroscopy (EDS) characterization studies were performed on an FEI Titan G2 60-300. The surface element compositions and valence states of $Li_{1+x}Cd_{x/2}Zr_{2-x/2}(PO_4)_3$ ($x = 0.5, 1, 1.5, 2$) and $CdZr_4(PO_4)_6$ powder were identified using X-ray photoelectron spectroscopy (XPS, Shimadzu AXI Sultra DLD) with Al Kα radiation. To analyze the surface characteristics of powder, Raman spectra analysis was performed at room temperature on a Thermo Scientific DXR3xi microscopic Raman spectrometer with a 532 nm laser and 10× microscope objective. Fourier transform infrared spectroscopy (FTIR) spectral data were obtained using a Fourier transform infrared spectrometer (Thermo Scientific Nicolet iS20) in the wavelength range of 400–4000 cm⁻¹.

2.4. Simulation and numerical analysis

The Vienna *Ab Initio* Simulation Package (VASP) was employed to perform all the density functional theory (DFT) calculations

This journal is © The Royal Society of Chemistry 2024

J. Mater. Chem. A, 2024, **12**, 4796–4805 | **4797**

within the generalized gradient approximation (GGA) using the Perdew, Burke, and Enzerhof (PBE) formulation.[27–29] The projected augmented wave (PAW) potentials were applied to describe the ionic cores and take valence electrons into account using a plane wave basis set with a kinetic energy cutoff of 450 eV.[30,31] Partial occupancies of the Kohn–Sham orbitals were allowed using the Gaussian smearing method and a width of 0.05 eV. The electronic energy was considered self-consistent when the energy change was smaller than 10^{-6} eV. A geometry optimization was considered convergent when the force change was smaller than 0.05 eV $Å^{-1}$. Grimme's DFT-D3 methodology was used to describe the dispersion interactions.[32] The equilibrium lattice constants of the $Li_3CdZr(PO_4)_3$ unit cell were optimized when using a $3 \times 3 \times 2$ Monkhorst–Pack k-point grid for Brillouin zone sampling. The climbing image-nudged elastic band method had been employed to calculate the H/Li ion migration barriers in the $Li_3CdZr(PO_4)_3$ structures.

3. Results and discussion

3.1. Carrier transport mechanism analysis

In order to explore the conduction mechanism of the $Li_3Cd_1Zr_1(PO_4)_3$ electrolyte material under fuel cell conditions, DFT theoretical computations based on VASP were adopted here to predict the ion transport trajectories. As $Li_3Cd_1Zr_1(PO_4)_3$ crystallizes in the orthorhombic system with the $Pnma$ space group, alternation of chains ZrO_6 and CdO_6 octahedra are linked together by PO_4 tetraheadra sharing oxygen vertices, whereas the Li+ ions are distributed in different sites. Some Li^+ ions are fixed in the skeleton structure to construct three-dimensional connected ion-transport channels, and other lithium ions migrate freely in the interconnected interstitial space.

In the fuel cell test conditions, a steady stream of hydrogen injection brings lots of H^+ ions to enter the interstitial space which has been filled by some Li^+ ions. Based on the climbing image-nudged elastic band method, both the proton and Li ions can move freely in the interstitial space within the 3D transport network as schematically illustrated in Fig. 1a and b. The migration path of lithium ions and protons in the 3D structure is obtained by simulation calculation, and it is clear that the proton migration path is shorter.

Further calculations of the migration barrier of H/Li ions on the migration route are shown in Fig. 1c. In the migration path from the 6b site to the 36f site, the migration barrier of protons is 0.23 eV lower than that of lithium ions (0.34 eV). The energy barrier of 230 meV for this migration route is close to the value reported in the previous research.[14,33] The maximum migration barrier of lithium ions is as high as 0.7 eV, while the proton is still at a low value of 0.2 eV in the 36f–18e path. Therefore, the proton possesses a lower migration barrier compared with lithium ions in the whole migration route, which indicates that the proton is the main transport carrier in the $Li_3CdZr(PO_4)_3$ material under fuel cell conditions.

To further demonstrate the ion hopping method in interstitial spaces, the detailed transition paths of protons and lithium ions are depicted in Fig. 1d and e. Here, three ions (Li^+/H^+) in different sites are selected to illustrate the cooperative hopping method, two in 36f sites and 1 in 6b site. The ion (Li^+/H^+) residing in the tetrahedral 36f site displaces the face-sharing octahedral 6b site. Li ions in 36f sites hop right along the surface of the polyhedron 18e site to the opposite tetrahedral 36f site, whereas the proton adopts the path of direct hopping through the polyhedron 18e site. Different transition modes explain the apparent barrier difference between the 36f and 18e sites even if the migration site is the same. The ion (Li^+/H^+) originally in the center of the octahedral 6b site is pushed to the tetrahedral 36f site on the right. Based on the same cooperative hopping mechanism, this kind of transition method can continue to propagate in the $Li_3CdZr(PO_4)_3$ network.

In general, the migration sites of the protons and lithium ions are the same, but the different migration modes lead to different path lengths, which directly affect the value of the migration energy barrier. Under fuel cell test conditions, the proton possesses the lower migration barrier and is considered the main carrier contributing to the ionic conductivity characteristics of the $Li_3CdZr(PO_4)_3$ cell device.

3.2. Phase and structural analysis

Based on the conclusion from the above theoretical calculations, we predicted that NASICON-type solid electrolyte would be a good conductor for proton transfer. Hence, the series $Li_{1+x}Cd_{x/2}Zr_{2-x/2}(PO_4)_3$ with different Li contents were successfully synthesized by the sol–gel method. The XRD patterns of $Li_{1+x}Cd_{x/2}Zr_{2-x/2}(PO_4)_3$ ($x = 0.5, 1, 1.5, 2$) and $CdZr_4(PO_4)_6$ samples are shown in Fig. 2a. The XRD pattern of the $CdZr_4(PO_4)_6$ sample is in good agreement with the olivine-type structure with the space group $R\bar{3}$ (PDF 45-0017) belonging to the trigonal system. No extra impurity phases are observed in the synthesized sample, confirming the successful single-phase structure. The diffraction peaks of $Li_{1+x}Cd_{x/2}Zr_{2-x/2}(PO_4)_3$ ($x = 0.5, 1, 1.5, 2$) samples conformed to crystal structures of $LiCdPO_4$ (PDF 81-0508) and $CdZr_4(PO_4)_6$ (PDF 45-0017), and some extra peaks are also detected and attributed to ZrO_2 (PDF 89-9069). The reason for the extra impure phase is probably that Li and P are both easy to volatilize in high temperature synthesis procedures.[34] With an increase in lithium element doping, the trigonal structure system of $CdZr_4(PO_4)_6$ is further transformed into the olivine-type structure of $LiCdPO_4$ with the $Pnma$ space group attributed to the orthorhombic system, and the content of the impure phase also decreases in this process, which creates a broader interstitial space for ions moving freely.

The morphology of the $CdZr_4(PO_4)_6$ and $Li_3Cd_1Zr_1(PO_4)_3$ samples characterized by the SEM method is shown in Fig. S1.† Both samples are made of nanoparticles smaller than 100 nm and the agglomeration is severe probably because of the insufficient grinding. Fig. 2b presents the HRTEM image of $Li_3Cd_1Zr_1(PO_4)_3$ powder. Clear lattice fringes with spacing distances of 3.59 Å and 3.10 Å could be observed, corresponding to the (111) and (211) crystal planes of the olivine-type structure consistent with the XRD results. As presented in Fig. 2c–g, high-angle annular dark-field (HAADF) image and corresponding EDS elemental mappings of $Li_3Cd_1Zr_1(PO_4)_3$ powder further

4798 | J. Mater. Chem. A, 2024, 12, 4796–4805
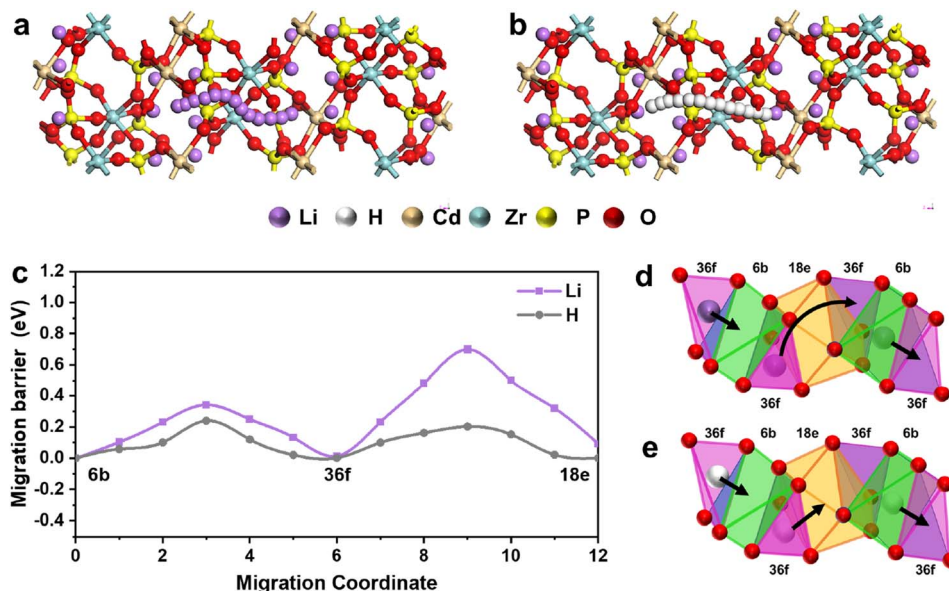
This journal is © The Royal Society of Chemistry 2024

Fig. 1 Transport trajectories for Li$^+$ ions (a) and H$^+$ ions (b) in the 3D Li$_3$Cd$_1$Zr$_1$(PO$_4$)$_3$ framework. (c) The migration barrier of proton and Li$^+$ ions between different sites under fuel cell conditions. Cooperative hopping of three Li$^+$ (d) and H$^+$ (e) on 36f–36f–6b sites in the Li$_3$Cd$_1$Zr$_1$(PO$_4$)$_3$ framework. Green octahedra: 6b sites, orange polyhedra: 18e sites, and purple tetrahedra: 36f sites.

confirm the characteristic of uniform distribution of elements. Due to the limitations of EDS technology, the distribution of Li element is not observed here. XPS characterization will be used to determine the existence of lithium in the following section.

3.3. XPS analysis

The XPS technology was adopted here to analyze the surface chemical valence states of the as-synthesized CdZr$_4$(PO$_4$)$_6$ and Li$_3$Cd$_1$Zr$_1$(PO$_4$)$_3$ samples. The presence of lithium in Li$_3$Cd$_1$-Zr$_1$(PO$_4$)$_3$ was determined using this technique. The recorded XPS spectra of P 2p, Li 1s, Zr 3d, and Cd 3d for the two sample powders are presented in Fig. 3.

As shown in Fig. 3a, the peaks located at binding energies of 412.07 eV (412.53 eV) and 405.33 eV (405.80 eV) are assigned to be the satellite peaks of Cd 3d$_{3/2}$ and Cd 3d$_{5/2}$, which are consistent with the previous report for Cd^{2+}.[35] Zr exists in a +4 valence state due to the couple of spin orbital peaks of Zr 3d$_{3/2}$ located at 184.24 eV (185.40 eV) and Zr 3d$_{5/2}$ at 181.95 eV (183.05 eV)[36] observed in Fig. 3b. As shown in Fig. 3c, the peak located at 133.31 eV (133.50 eV) is assigned to be the characteristic peak of P 2p, which characterizes the +5 valence state.[37] In comparison to CdZr$_4$(PO$_4$)$_6$, the peaks of Li$_3$Cd$_1$Zr$_1$(PO$_4$)$_3$ in cation-site elements (Cd, Zr and P) all shift towards higher binding energy due to the complexed ionic coordination environment caused by lithium-ion doping. However, the binding energy
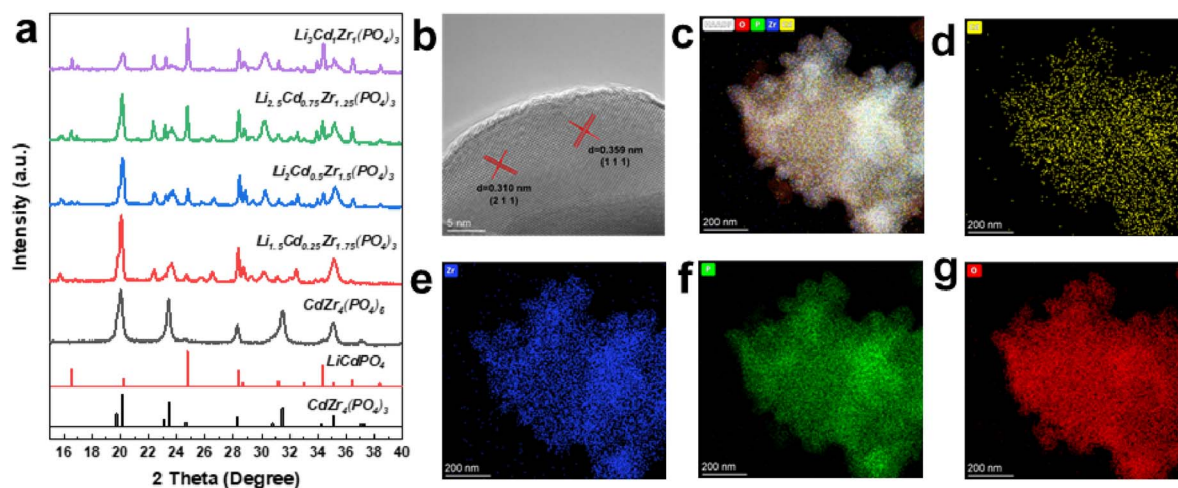

Fig. 2 The XRD analysis of Li$_{1+x}$Cd$_{x/2}$Zr$_{2-x/2}$(PO$_4$)$_3$ (x = 0.5, 1, 1.5, 2) and CdZr$_4$(PO$_4$)$_6$ powder (a), HRTEM image (b), HAADF-TEM image (c) and the corresponding EDS elemental mappings (d–g) of Li$_3$Cd$_1$Zr$_1$(PO$_4$)$_3$ powder.
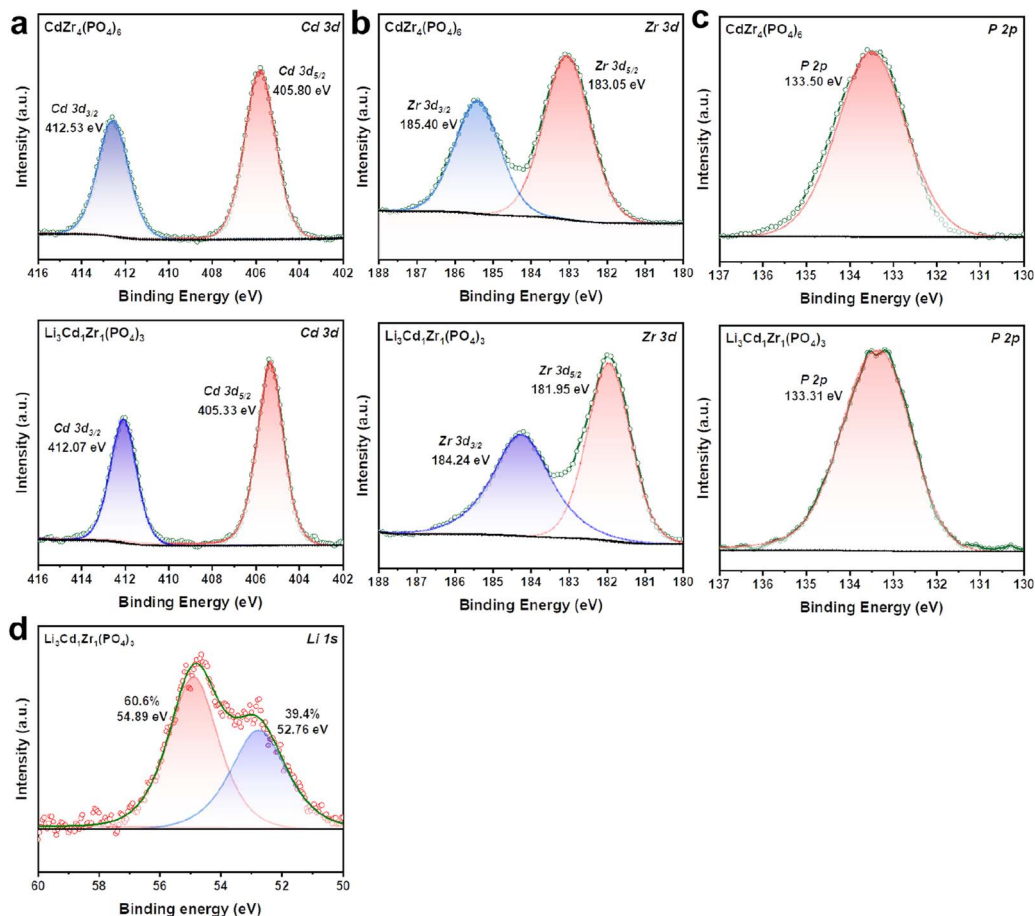
This journal is © The Royal Society of Chemistry 2024

J. Mater. Chem. A, 2024, 12, 4796–4805 | 4799

Fig. 3 XPS spectra of (a) Cd 3d, (b) Zr 3d, and (c) P 2p for $CdZr_4(PO_4)_6$ and $Li_3Cd_1Zr_1(PO_4)_3$ samples. XPS spectra of (d) Li 1s for the $Li_3Cd_1Zr_1(PO_4)_3$ sample.

differences between doublets are very close, indicative of no detectable change in the spin orbit components. Fig. 3d confirms the presence of Li^+ with a characteristic binding energy of 54.89 eV attributed to Li_3PO_4 (ref. 38) and 52.76 eV attributed to Li_2O (ref. 39) in $Li_3Cd_1Zr_1(PO_4)_3$, which indicates the successful introduction of Li into the olivine type structure.

The deconvoluted spectrum of O 1s was collected to further analyze the oxygen vacancy depicted in Fig. S2.† It includes three characteristic peaks corresponding to lattice oxygen (O_L), oxygen vacancy (O_v), and chemically adsorbed oxygen species (O_a).[40] O_v is ascribed to defect oxide which is beneficial for ionic transport. O_a is the chemisorbed oxygen species which are easily liberated at fuel cell operating temperature. It is worth noting that O_v occupies the dominant position in $Li_3Cd_1Zr_1(PO_4)_3$ while O_L is dominant in $CdZr_4(PO_4)_6$, illustrating an apparent increment of surface oxygen vacancies in the $Li_3Cd_1Zr_1(PO_4)_3$ sample attributed to the doping of lower valent Li^+.

3.4. Raman spectra analysis

Raman spectroscopy is used to verify the lithium incorporation in the olivine-type structure. Raman spectra of both $CdZr_4(PO_4)_6$ and $Li_3Cd_1Zr_1(PO_4)_3$ samples were measured and are presented in Fig. 4, which agree well with the assignments reported in the

previous study.[41–44] Considering that the lithium atoms located in sites with inversion symmetry are not spectroscopically active, lithium vibrations are hard to be identified. Here an attempt is made to indirectly prove the successful doping of lithium based on the movement of other bonds. The bands located above 400 cm^{-1} are attributed to internal modes originating from the intramolecular vibrations of the $(PO_4)^{3-}$ anion.
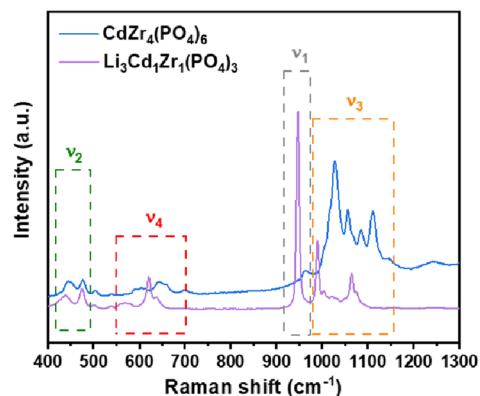

Fig. 4 Raman spectra of $CdZr_4(PO_4)_6$ and $Li_3Cd_1Zr_1(PO_4)_3$ samples.

4800 | *J. Mater. Chem. A*, 2024, **12**, 4796–4805

This journal is © The Royal Society of Chemistry 2024

Paper

Four bands are observed between 1100 and 900 cm^{-1} in the Raman spectrum of $Li_3Cd_1Zr_1(PO_4)_3$. The salient Raman signature with the highest intensity at 948 cm^{-1} is assigned to the symmetric P–O stretching vibration band of v_1. The antisymmetric stretching bands of the PO_4^{3-} anion ($v3$) appear in the bands between 990 and 1100 cm^{-1}. Raman bands between 550 and 700 cm^{-1} are ascribed to v_4 of O–P–O asymmetric bending vibrations. The frequencies located at 440 cm^{-1} and 476 cm^{-1} are related to the O–P–O symmetric bending vibration of v_2. For the undoped $CdZr_4(PO_4)_6$ sample, Raman bands observed at 963 cm^{-1} (v_1), 448 cm^{-1} and 478 cm^{-1} (v_2), 1000–1150 cm^{-1} (v_3) and 550–700 cm^{-1} (v_4) belong to the functional group $(PO_4)^{3-}$. The Raman peaks of $Li_3Cd_1Zr_1(PO_4)_3$ samples red-shift in comparison to the undoped $CdZr_4(PO_4)_6$ probably because the incorporation of Li into the $CdZr_4(PO_4)_6$ structure creates lattice disorder, hence confirming the successful incorporation of lithium.

3.5. Electrochemical analysis

The $Li_{1+x}Cd_{x/2}Zr_{2-x/2}(PO_4)_3$ ($x = 0.5, 1, 1.5, 2$) and $CdZr_4(PO_4)_6$ electrolyte samples are applied to fuel cells to conduct further study. As presented in Fig. 5a, the I–V and I–P performances of the fuel cell device with different solid electrolytes are assessed and compared in H_2/air at 460–550 °C. All the cell devices exhibit about 1.0 V high OCVs at 550 °C, suggesting that electronic leakage could be negligible. The pristine $CdZr_4(PO_4)_6$ device demonstrates a maximum peak power density (P_{max}) of 402 mW cm^{-2} at 550 °C. However, the electrochemical performance is improved with an increase in lithium introduction to $Li_{1+x}Cd_{x/2}Zr_{2-x/2}(PO_4)_3$ ($x = 0.5, 1, 1.5, 2$) materials, and the $Li_3Cd_1Zr_1(PO_4)_3$ fuel cell reaches a maximum P_{max} of 815 mW cm^{-2} at 550 °C, which is two times higher than that of the $CdZr_4(PO_4)_6$ cell. The electrochemical performance of the $Li_{1+x}Cd_{x/2}Zr_{2-x/2}(PO_4)_3$($x = 0.5, 1, 1.5, 2$) cells is apparently higher than that of the pristine $CdZr_4(PO_4)_6$ device, which may be because of the higher ionic conductivity of $Li_{1+x}Cd_{x/2}Zr_{2-x/2}(PO_4)_3$($x = 0.5, 1, 1.5, 2$) beneficial from lithium doping creating more ion migration channels. As shown in Fig. 5b, the $Li_3Cd_1Zr_1(PO_4)_3$ cell device yields a P_{max} of 677 mW cm^{-2}, 530 mW cm^{-2}, and 421 mW cm^{-2} at 520 °C, 490 °C and 460 °C, respectively. It is attractive that the $Li_3Cd_1Zr_1(PO_4)_3$ cell device shows considerable OCV and power density even at 460 °C, which indicates that this material is the potential electrolyte for IT-PCFCs.

The electrochemical impedance spectroscopy (EIS) plots for the $Li_{1+x}Cd_{x/2}Zr_{2-x/2}(PO_4)_3$ ($x = 0.5, 1, 1.5, 2$) and $CdZr_4(PO_4)_6$ device were recorded under H_2/air and are shown in Fig. 5c and d. The experimental EIS data were fitted with an equivalent circuit of R_o (R_1CPE_1) (R_2CPE_2). R represents the resistance, which can be further subdivided into three major parts consisting of the ohmic resistance R_o, anode polarization resistance R_1 and cathode polarization resistance R_2, respectively. CPE represents the constant phase element for a non-ideal capacitor. The simulation results of $Li_{1+x}Cd_{x/2}Zr_{2-x/2}(PO_4)_3$ ($x = 0.5, 1, 1.5, 2$) and $CdZr_4(PO_4)_6$ cell device are summarized in Tables S1–S2.† The $Li_3Cd_1Zr_1(PO_4)_3$ cell device yields a minimum ohmic

resistance of 0.45 Ω cm^2, and the increase of lithium doping leads to a lower R_o than that of the pristine $CdZr_4(PO_4)_6$ device (0.96 Ω cm^2) at 550 °C, which coincides with the electrochemical performance. Table S2† lists the simulation results of the Li_3-$Cd_1Zr_1(PO_4)_3$ cell under H_2/air conditions at 460–550 °C. The ohmic resistance R_o decreases from 0.59 to 0.45 Ω cm^2 when the temperature increases from 460 to 550 °C, indicating the facilitated electrode reaction process of the $Li_3Cd_1Zr_1(PO_4)_3$ cell.

To further confirm the superior ionic conduction of the $Li_3Cd_1Zr_1(PO_4)_3$ cell at intermediate temperatures, the ionic conductivities of the five materials were calculated and are compared in Fig. 5e and f. The ionic conductivity is calculated according to the relation $\sigma = L/RS$, where L is the thickness of the electrolyte pellet, R is the resistance from the EIS simulation results or the intermediate ohmic polarization region of the I–V polarization curves, and S is the active area of the electrolyte pellet. The cross-sectional view of the fabricated fuel cell device is shown in Fig. S3† and the thickness of the electrolyte pellet is 0.55 mm. The ionic conductivity calculated from EIS and I–V curves of the $Li_{1+x}Cd_{x/2}Zr_{2-x/2}(PO_4)_3$ ($x = 0.5, 1, 1.5, 2$) and $CdZr_4(PO_4)_6$ device is presented in Fig. 5e. The $Li_3Cd_1Zr_1(PO_4)_3$ cell acquires the best ionic conductivity values of 0.165 S cm^{-1} at 550 °C, which is two times higher than that of the pristine $CdZr_4(PO_4)_6$ device. Other $Li_{1+x}Cd_{x/2}Zr_{-x/2}(PO_4)_3$ ($x = 0.5, 1, 1.5$) devices with lithium doping also show high ionic conductivity with values of 0.158 S cm^{-1}, 0.136 S cm^{-1} and 0.122 S cm^{-1} respectively. The ionic conductivity values acquired by the EIS results and I–V curves are reliable due to the small numerical difference. With an increase in Li content, the changed structure creates a broader interstitial space for ion transport, which contributes to the improvement of ion conductivity.

Moreover, the activation energies for ionic conduction of the $Li_3Cd_1Zr_1(PO_4)_3$ cell at different temperatures are calculated from the slops of the Arrhenius plots. As shown in Fig. 5f, the $Li_3Cd_1Zr_1(PO_4)_3$ cell obtains a low activation energy of 0.372 eV from the EIS results and 0.396 eV from I–V curves. The low activation energy of the $Li_3Cd_1Zr_1(PO_4)_3$ cell is close to that of traditional proton electrolytes in such a temperature range. Lower activation energy provides higher fuel cell electrochemical performance at medium temperatures. Therefore, it can be speculated that the high performance of the Li_3Cd_1-$Zr_1(PO_4)_3$ material at 460–550 °C may be ascribed to contribution of proton conduction, which is in good agreement with those obtained by the DFT simulation results.

The ionic conductivities of as-prepared $Li_3Cd_1Zr_1(PO_4)_3$ electrolyte and other conventional oxygen ion conductors $Zr_{0.92}Y_{0.08}O_{1.96}$(YSZ),[45] $Ce_{0.9}Gd_{0.1}O_{1.95}$(GDC),[46] and $(Bi_{0.95}$-$Zr0.05)_{0.85}Y_{0.15}O_{1.5+\delta}$ (BiZrY),[47] proton conductors $BaZr_{0.1}Ce_{0.7}$-$Y_{0.1}Yb_{0.1}O_{3-\delta}$ (BZCYYb)[48] and hydride conductors (BaH_2)[49] are presented in Fig. 6. The ionic conductivity of $Li_3Cd_1Zr_1(PO_4)_3$ electrolyte is significantly higher than that of oxygen ion conductors in the medium temperature range (460–550 °C). In comparison to proton conductors BZCYYb and hydride conductors BaH_2 subjected to the same temperature conditions, $Li_3Cd_1Zr_1(PO_4)_3$ electrolyte also exhibits similar superior conductivity.
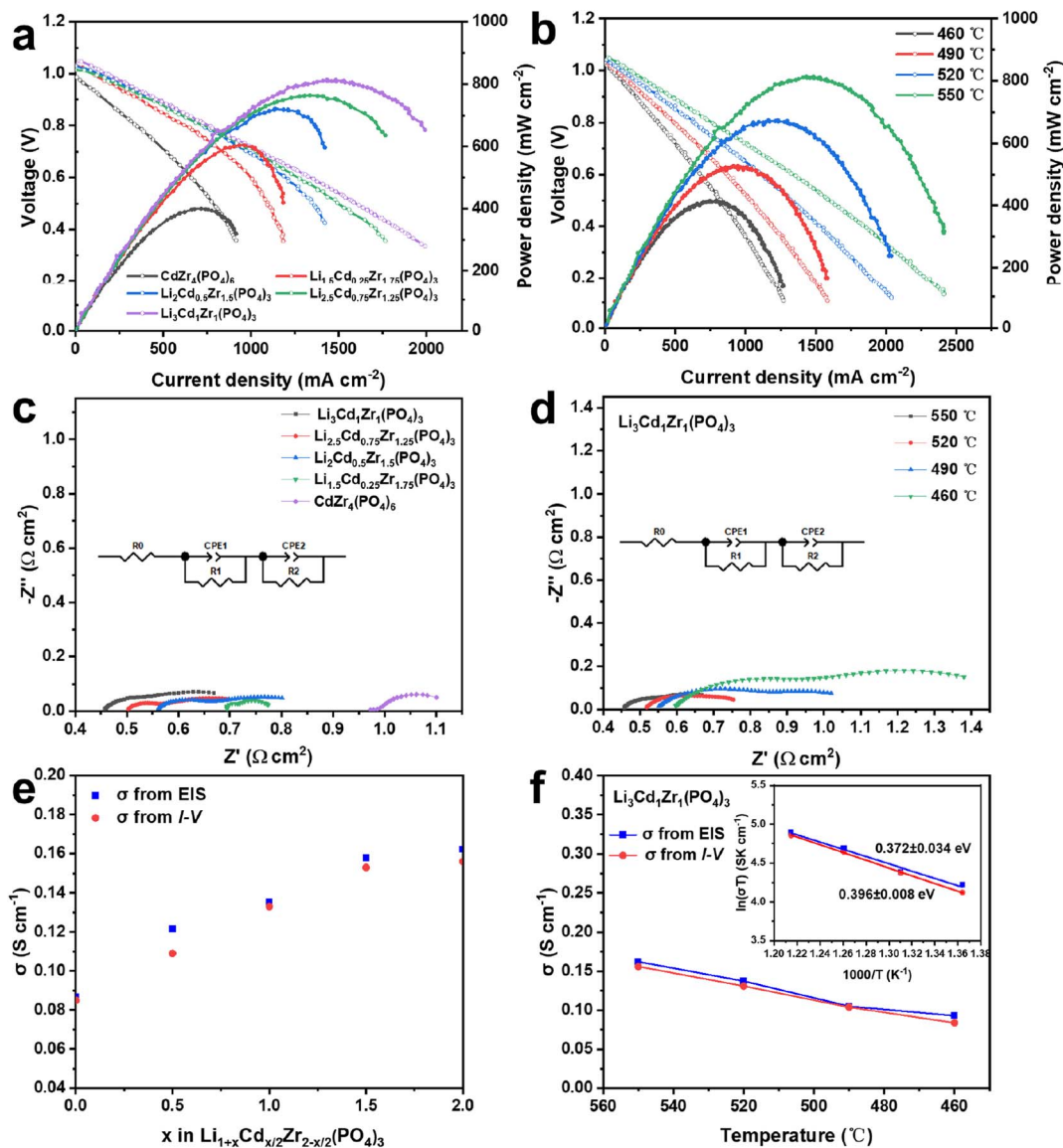
Fig. 5 (a) Electrical performance of fuel cells based on the $Li_{1+x}Cd_{x/2}Zr_{2-x/2}(PO_4)_3$ ($x = 0.5, 1, 1.5, 2$) and $CdZr_4(PO_4)_6$ samples at 550 °C. (b) Electrical performance of fuel cells based on the $Li_3Cd_1Zr_1(PO_4)_3$ sample at 460–550 °C. (c) Electrochemical impedance spectroscopy (EIS) plots of the $Li_{1+x}Cd_{x/2}Zr_{2-x/2}(PO_4)_3$ ($x = 0.5, 1, 1.5, 2$) and $CdZr_4(PO_4)_6$ device at 550 °C. (d) Electrochemical impedance spectroscopy (EIS) plots of the $Li_3Cd_1Zr_1(PO_4)_3$ sample at 460–550 °C. (e) Ionic conductivity of the $Li_{1+x}Cd_{x/2}Zr_{2-x/2}(PO_4)_3$ ($x = 0.5, 1, 1.5, 2$) and $CdZr_4(PO_4)_6$ device from EIS and $I-V$ curves. (f) Activation energy calculated of the $Li_{1+x}Cd_{x/2}Zr_{2-x/2}(PO_4)_3$ ($x = 0.5, 1, 1.5, 2$) and $CdZr_4(PO_4)_6$ device from EIS and $I-V$ curves.

3.6. Carrier transport experiment analysis

The DFT calculation results demonstrated that the proton is the main carrier in $Li_3Cd_1Zr_1(PO_4)_3$ from a simulation aspect, and the proton conduction mechanism was further investigated by the following experiments.

In order to characterize the type of ions ($Li^+/H^+/O^{2-}$) responsible for the fuel cell performance, $I-t$ curves of the Ag/$Li_3Cd_1Zr_1(PO_4)_3$/Ag device in N_2/N_2, H_2/H_2 and air/air atmospheres at 550 °C were recorded with a potential of 1 V. As depicted in Fig. 7a, the current in the H_2 atmosphere yields a higher value, while the current in the air/air atmosphere is slightly higher than that in the N_2 atmosphere. The H^+ conductivity of the Ag/$Li_3Cd_1Zr_1(PO_4)_3$/Ag device exposed to the

H_2 atmosphere is calculated to be 2.94×10^{-5} s cm^{-2} because hydrogen gas served as the proton source. Under N_2 and air atmospheres, Li^+ and O^{2-} as the transport carriers in Li_3Cd_1-$Zr_1(PO_4)_3$ demonstrate a conductivity of 2.62×10^{-5} and 2.66×10^{-5} s cm^{-2}, respectively. The transport capacities of oxygen and lithium ions are similar and lower than that of protons, which indicates that protons are the dominant transport carriers responsible for $Li_3Cd_1Zr_1(PO_4)_3$ cell performance. More detailed experimental comparisons of the contributions of the three ions are presented below.

Fourier transform infrared (FTIR) spectroscopy was performed to compare the functional groups of $Li_3Cd_1Zr_1(PO_4)_3$ before and after the performance test. As depicted in Fig. 7b, the

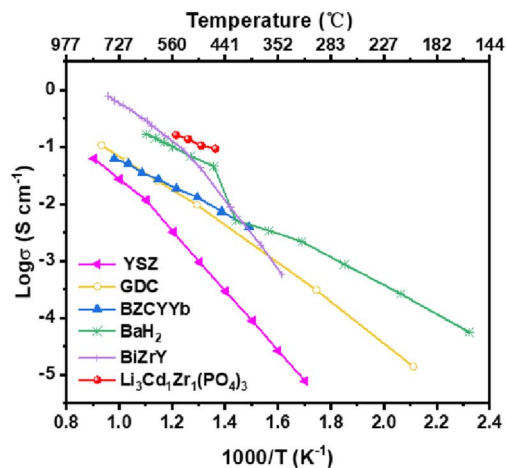4802 | J. Mater. Chem. A, 2024, 12, 4796–4805

This journal is © The Royal Society of Chemistry 2024

Fig. 6 Ionic conductivities of the $Li_3Cd_1Zr_1(PO_4)_3$ material and other well-known ionic conductors (oxygen ion conductors: $Zr_{0.92}Y_{0.08}O_{1.96}$(YSZ),[45] $Ce_{0.9}Gd_{0.1}O_{1.95}$(GDC),[46] and $(Bi_{0.95}Zr0.05)_{0.85}Y_{0.15}O_{1.5+\delta}$ (BiZrY).[47] Proton conductors: $BaZr_{0.1}Ce_{0.7}Y_{0.1}Yb_{0.1}O_{3-\delta}$ (BZCYYb)[48] and hydride conductors (BaH_2)[49]) in the previous report.

new band observed at 3409 cm^{-1} after the test is attributed to the O–H bond in the hydroxyl group.[50] This indicates that protons insert and may transfer as O–H carriers in the $Li_3Cd_1Zr_1(PO_4)_3$ electrolyte under the cell environment. Other bands at 540–630 cm^{-1} and 410–470 cm^{-1} are assigned to the variable angles of PO_4 and the band located at 1037 cm^{-1} corresponds to the asymmetric stretching vibration of PO_43-.[51] Bands located at

1442 cm^{-1} and 866 cm^{-1} are ascribed to CO_3^{2-} modes from the CO_2 molecules on the sample surfaces.[52] The FTIR results indicate that proton transfer exists in $Li_3Cd_1Zr_1(PO_4)_3$ under cell conditions.

Hydrogen concentration cell (HCC) and oxygen concentration cell (OCC) tests were further carried out to demonstrate the proportion of proton and oxygen conduction in the $Li_3Cd_1Zr_1(PO_4)_3$ material. The migration number is calculated as the ratio of observed voltage and theoretical voltage (calculated according to the Nernst equation). Both sides of the electrolyte pellet were painted with Ag paste, and air and $5\%O_2 + 95\%Ar$ were supplied to Ag electrodes in the OCC test. The OCC voltage was hardly detected and the oxygen migration number was about zero, indicative of negligible oxygen conduction in $Li_3Cd_1Zr_1(PO_4)_3$. The $Ag/Li_3Cd_1Zr_1(PO_4)_3/Ag$ cell was then measured in a pure H_2 and $5\%H_2 + 95\%Ar$ atmosphere for the HCC test. As shown in Fig. 7c, the H^+ transfer number is between 55% and 80% at 400–610 °C, indicating that proton conduction accounts for a high proportion in $Li_3Cd_1Zr_1(PO_4)_3$. As silver is not an ideal electrode for cells, the real transfer number value is higher. However, it is possible for Li^+ ion conduction to make contributions under hydrogen concentration cell conditions, which requires further discussion.

After excluding the contribution of oxygen ions, the lithium-ion conductivity of $Li_3Cd_1Zr_1(PO_4)_3$ was analyzed using the EIS results of the $Ag/Li_3Cd_1Zr_1(PO_4)_3/Ag$ cell in air. As shown in Fig. S4a,† the lithium ion conductivity of the $Li_3Cd_1Zr_1(PO_4)_3$ pellet is 3.2×10^{-4} S cm^{-1} at 550 °C, which is much lower than
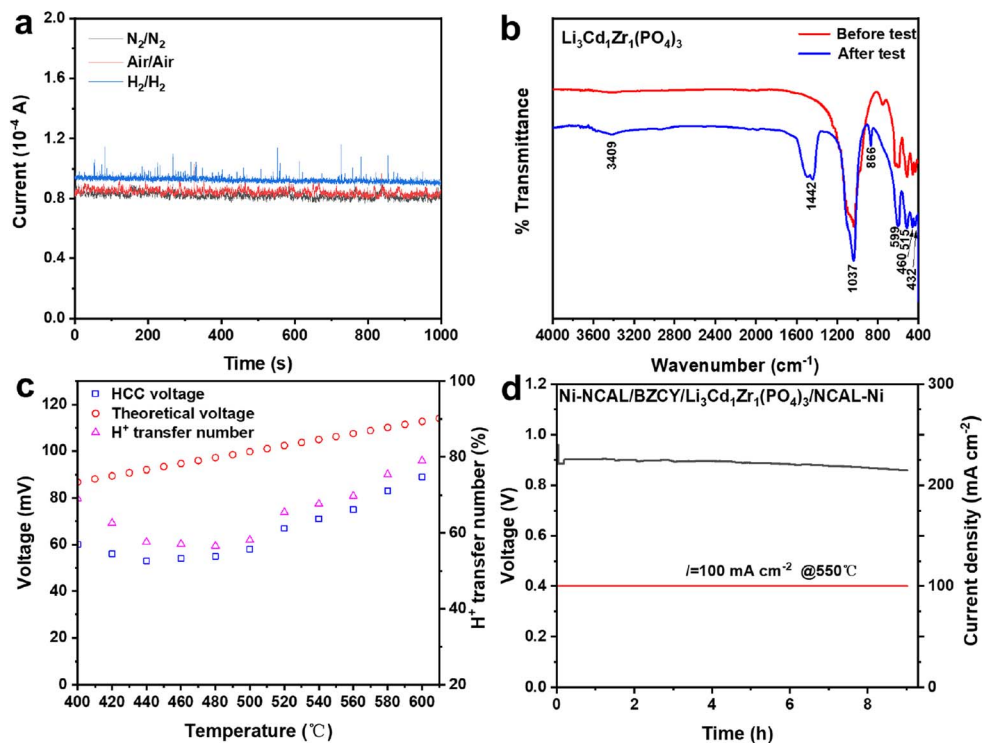
Fig. 7 (a) $I-t$ curves of the $Ag/Li_3Cd_1Zr_1(PO_4)_3/Ag$ device measured in different atmospheres at 550 °C. (b) FTIR spectra of $Li_3Cd_1Zr_1(PO_4)_3$ before and after the performance test. (c) The observed OCV, theoretical OCV and H^+ transfer number from the HCC test. (d) Durability performance test of the $Li_3Cd_1Zr_1(PO_4)_3$ device with the protection layer at 550 °C.

that of the $Li_3Cd_1Zr_1(PO_4)_3$ cell in a fuel cell atmosphere (0.165 S cm^{-1}). The EIS results indicate that the lithium ion conductivity of $Li_3Cd_1Zr_1(PO_4)_3$ can be excluded in a fuel cell environment. Furthermore, the durability test was performed with a constant current density of 100 mA cm^{-2} at 550 °C. As depicted in Fig. S4b,† the voltage of the $Li_3Cd_1Zr_1(PO_4)_3$ cell decays suddenly after about 0.9 hours likely due to its partial reduction on the hydrogen side. $BaZrO_3$-based materials have good compatibility between electrolyte and the anode in fuel cell environments and hence proton conductor $BaZr_{0.1}Ce_{0.7}$-$Y_{0.2}O_{3-\delta}$ (BZCY) was used as the protection layer here.[21,53] As depicted in Fig. 7d, the durability performance of the Li_3Cd_1-$Zr_1(PO_4)_3$ cell with the BZCY protection layer is significantly improved to 9 hours. Both electrodes and electrolytes containing lithium ions may serve as sources to contribute to Li-ion conductivity, and the idealized case of migration of all lithium ions was considered here. Based on the maximum amount of charge carried by all lithium ions and the constant current density 100 mA cm^{-2}, the maximum durability time that lithium ions can contribute in the $Li_3Cd_1Zr_1(PO_4)_3$ cell is calculated to be about 1.8 h. Because most Li$^+$ ions are fixed in the structure and mobile ions are in the minority, the lithium ions in NCAL electrodes and $Li_3Cd_1Zr_1(PO_4)_3$ electrolytes cannot be completely exhausted and no lithium-ion source will be supplemented after the migration of all mobile Li ions, so its actual contribution to performance is smaller. Therefore, the contribution of lithium ions in performance of the $Li_3Cd_1Zr_1(PO_4)_3$ cell device can be neglected here. The durability test was carried out in the laboratory stage and the novel $Li_3Cd_1Zr_1(PO_4)_3$ electrolyte material needs mature assembly and testing processes to complete the long-term durability test.

The above experiment results demonstrate that the existence of Li$^+$/O^{2-} can be neglected and proton conduction is dominant in $Li_3Cd_1Zr_1(PO_4)_3$ under fuel cell conditions, corresponding to the simulation results.

4. Conclusions

Overall, the NASICON-structure proton conductor $Li_{1+x}Cd_{x/2}Zr_{2-x/2}(PO_4)_3$ (x = 0.5, 1, 1.5, 2) material derived from $CdZr_4(PO_4)_6$ is synthesized and related to electrochemical devices. An increase in the introduction of lithium in $CdZr_4(PO_4)_6$ leads to a structural change from a trigonal to an orthorhombic system, which creates more 3D interstitial space for ions moving freely which is beneficial for ion conductivity. Focusing on the understanding of the proton conduction mechanism, the migration method of Li$^+$/H$^+$ in interstitial space of the $Li_3Cd_1Zr_1(PO_4)_3$ structure has been investigated *via* DFT simulation. The proton has the smaller migration barrier and is shown as the main transport carrier in the $Li_3Cd_1Zr_1(PO_4)_3$ material under fuel cell conditions, which is also confirmed by the experiments that exclude the contributions of lithium ions and oxygen ions. Among five electrolyte samples, the $Li_3Cd_1Zr_1(PO_4)_3$ single cell device exhibits excellent electrochemical performance with a peak power density of 815 mW cm^{-2}, an ionic conductivity of 0.165 S cm^{-1} and an activation energy of 0.372 eV at 550 °C. Notably, the ionic conductivity of

$Li_3Cd_1Zr_1(PO_4)_3$ outperforms that of other conventional oxygen ion/proton/hydride conductors, showing great application potential in fuel cell electrolyte. The novel proton transport mechanism provides important insights into rational design of proton conductors for intermediate temperature fuel cells and other electrochemical systems.

Author contributions

Conceptualization: Xiuxiu Li and Faze Wang. Formal analysis and methodology: Xiuxiu Li, Enyi Hu and Faze Wang. Project administration, funding acquisition and supervision: Jun Wang and Faze Wang. Resources and investigation: Bin Zhu. Writing—original draft: Xiuxiu Li and Enyi Hu. Software and writing—review and editing: Faze Wang and Peter Lund.

Conflicts of interest

There are no conflicts to declare.

Acknowledgements

References

1 S. Zarabi Golkhatmi, M. I. Asghar and P. D. Lund, *Renewable Sustainable Energy Rev.*, 2022, **161**, 112339.

2 F. Ramadhani, M. A. Hussain, H. Mokhlis and S. Hajimolana, *Renewable Sustainable Energy Rev.*, 2017, **76**, 460–484.

3 M. Singh, D. Zappa and E. Comini, *Int. J. Hydrogen Energy*, 2021, **46**, 27643–27674.

4 S. P. Jiang, *Electrochem. Energy Rev.*, 2022, **5**, 21.

5 Z. Li, M. Li and Z. Zhu, *Electrochem. Energy Rev.*, 2022, **5**, 263–311.

6 N. Wang, C. Tang, L. Du, R. Zhu, L. Xing, Z. Song, B. Yuan, L. Zhao, Y. Aoki and S. Ye, *Adv. Energy Mater.*, 2022, **12**, 1–29.

7 M. Liang, Y. Zhu, Y. Song, D. Guan, Z. Luo, G. Yang, S. P. Jiang, W. Zhou, R. Ran and Z. Shao, *Adv. Mater.*, 2022, **34**, 1–9.

8 I. Zvonareva, X. Z. Fu, D. Medvedev and Z. Shao, *Energy Environ. Sci.*, 2022, **15**, 439–465.

9 M. T. Ahsan, Z. Ali, M. Usman and Y. Hou, *Carbon Energy*, 2022, **4**, 776–819.

10 Q. Zhou, L. Wang, W. Li, K. Zhao, M. Liu, Q. Wu, Y. Yang, G. He, I. P. Parkin, P. R. Shearing, D. J. L. Brett, J. Zhang and X. Sun, *Sodium Superionic Conductors (NASICONs) as Cathode Materials for Sodium-Ion Batteries*, Springer Singapore, 2021, vol. 4.

11 M. Hou, F. Liang, K. Chen, Y. Dai and D. Xue, *Nanotechnology*, 2020, **31**, 132003.

4804 | *J. Mater. Chem. A*, 2024, **12**, 4796–4805

This journal is © The Royal Society of Chemistry 2024

12 V. Soundharrajan, S. Nithiananth, K. Sakthiabirami, J. H. Kim, C. Y. Su and J. K. Chang, *J. Mater. Chem. A*, 2022, **10**, 1022–1046.

13 I. Hanghofer, B. Gadermaier, A. Wilkening, D. Rettenwander and H. M. R. Wilkening, *Dalton Trans.*, 2019, **48**, 9376–9387.

14 Y. Xiao, K. J. Jun, Y. Wang, L. J. Miara, Q. Tu and G. Ceder, *Adv. Energy Mater.*, 2021, **11**, 2101437.

15 R. Lan and S. Tao, *Adv. Energy Mater.*, 2014, **4**, 1301683.

16 L. Fan and P. C. Su, *J. Power Sources*, 2016, **306**, 369–377.

17 P. G. Komorowski, S. A. Argyropoulos, R. G. V. Hancock, J. Gulens, P. Taylor, J. D. Canaday, A. K. Kuriakose, T. A. Wheat and A. Ahmad, *Solid State Ionics*, 1991, **48**, 295–301.

18 L. Truong and V. Thangadurai, *Chem. Mater.*, 2011, **23**, 3970–3977.

19 L. Truong and V. Thangadurai, *Inorg. Chem.*, 2012, **51**, 1222–1224.

20 F. Chen, D. Liao, X. Pan, G. Lin and K. Peng, *Ceram. Int.*, 2022, **48**, 11304–11312.

21 T. Wei, L. A. Zhang, Y. Chen, P. Yang and M. Liu, *Chem. Mater.*, 2017, **29**, 1490–1495.

22 L. Sebastian, R. S. Jayashree and J. Gopalakrishnan, *J. Mater. Chem.*, 2003, **13**, 1400–1405.

23 T. Matsui, T. Ozeki, K. Miyazaki, S. Nagasaka, H. Muroyama, K. Imagawa, Y. Okada and K. Eguchi, *J. Mater. Chem. A*, 2023, **11**, 18207–18212.

24 I. A. Stenina, I. Y. Pinus, A. I. Rebrov and A. B. Yaroslavtsev, *Solid State Ionics*, 2004, **175**, 445–449.

25 I. A. Stenina, M. N. Kislitsyn, N. A. Ghuravlev and A. B. Yaroslavtsev, *Mater. Res. Bull.*, 2008, **43**, 377–383.

26 Y. Lu, E. Hu, M. Yousaf, L. Ma, J. Wang, F. Wang and P. Lund, *Energy Fuels*, 2022, **36**, 15154–15164.

27 J. P. Perdew, K. Burke and M. Ernzerhof, *Phys. Rev. Lett.*, 1996, **77**, 3865–3868.

28 D. Joubert, *Phys. Rev. B: Condens. Matter Mater. Phys.*, 1999, **59**, 1758–1775.

29 G. Kresse and J. Furthmüller, *Phys. Rev. B: Condens. Matter Mater. Phys.*, 1996, **54**, 11169–11186.

30 S. Grimme, J. Antony, S. Ehrlich and H. Krieg, *J. Chem. Phys.*, 2010, **132**, 154104.

31 P. E. Blöchl, *Phys. Rev.*, 1994, **50**, 17953–17979.

32 G. Henkelman, B. P. Uberuaga and H. Jónsson, *J. Chem. Phys.*, 2000, **113**, 9901–9904.

33 B. Lang, B. Ziebarth and C. Elsässer, *Chem. Mater.*, 2015, **27**, 5040–5048.

34 A. La Monaca, G. Girard, S. Savoie, H. Demers, G. Bertoni, S. Krachkovskiy, S. Marras, E. Mugnaioli, M. Gemmi, D. Benetti, A. Vijh, F. Rosei and A. Paolella, *J. Mater. Chem. A*, 2021, **9**, 13688–13696.

35 K. Mohanraj, J. H. Chang, D. Balasubramanian, J. Chandrasekaran, R. Marnadu, B. Babu, N. Senthil Kumar and S. Chandrasekar, *J. Alloys Compd.*, 2021, **888**, 161568.

36 M. Wang, K. Wang, X. Huang, T. Zhou, H. Xie and Y. Ren, *Ceram. Int.*, 2020, **46**, 28490–28498.

37 L. Zhang, Y. Liu, Y. Wang, X. Li and Y. Wang, *Appl. Surf. Sci.*, 2021, **557**, 149838.

38 H. Li, W. Jiang, W. Ma, H. Qu and Q. Zhong, *Chem. Eng. Commun.*, 2016, **203**, 339–344.

39 Q. Liu, D. Zhou, D. Shanmukaraj, P. Li, F. Kang, B. Li, M. Armand and G. Wang, *ACS Energy Lett.*, 2020, **5**, 1456–1464.

40 J. He, Y. Xu, P. Shao, L. Yang, Y. Sun, Y. Yang, F. Cui and W. Wang, *Chem. Eng. J.*, 2020, **394**, 124912.

41 Y. Bai, Y. Yin, J. Yang, C. Qing and W. Zhang, *J. Raman Spectrosc.*, 2011, **42**, 831–838.

42 T. Choudhury, E. Kumi-Barimah, P. Parameswaran Nampi, G. M. Kale and G. Jose, *Mater. Sci. Eng., B*, 2022, **277**, 115582.

43 G. B. Nair and S. J. Dhoble, *RSC Adv.*, 2015, **5**, 49235–49247.

44 A. Djemal, B. Louati and K. Guidara, *J. Mater. Sci.: Mater. Electron.*, 2017, **28**, 13806–13813.

45 E. Conductivity and R. Region, *J. Am. Ceram. Soc.*, 1952, **69**, 2–5.

46 B. C. H. Steele, *Solid State Ionics*, 2000, **129**, 95–110.

47 A. A. Yaremchenko, V. V. Kharton, E. N. Naumovich, A. A. Tonoyan and V. V. Samokhval, *J. Solid State Electrochem.*, 1998, **2**, 308–314.

48 L. Yang, S. Wang, K. Blinn, M. Liu, Z. Liu, Z. Cheng and M. Liu, *Science*, 2009, **326**, 126–129.

49 M. C. Verbraeken, C. Cheung, E. Suard and J. T. S. Irvine, *Nat. Mater.*, 2015, **14**, 95–100.

50 X. Sun and Y. Li, *Chem.–Eur. J.*, 2003, **9**, 2229–2238.

51 N. K. Anuar, S. B. R. S. Adnan and N. S. Mohamed, *Ceram. Int.*, 2014, **40**, 13719–13727.

52 E. Portillo, T. R. Reina, M. Cano, F. Vega and B. Navarrete, *Solid State Ionics*, 2019, **341**, 115039.

53 H. Wang, E. Hu, B. Zhu, Y. Wu and Q. Fan, *J. Power Sources*, 2023, **580**, 233464.

This journal is © The Royal Society of Chemistry 2024

J. Mater. Chem. A, 2024, **12**, 4796–4805 | **4805**